



**HAL**  
open science

## Miscible displacement fronts of shear thinning fluids inside rough fractures.

Alejandro Boschan, Harold Auradou, Irene Ippolito, Ricardo Chertcoff,  
Jean-Pierre Hulin

► **To cite this version:**

Alejandro Boschan, Harold Auradou, Irene Ippolito, Ricardo Chertcoff, Jean-Pierre Hulin. Miscible displacement fronts of shear thinning fluids inside rough fractures.. Water Resources Research, 2007, 43, pp.W03438. 10.1029/2006WR005324 . hal-00091346

**HAL Id: hal-00091346**

**<https://hal.science/hal-00091346>**

Submitted on 5 Sep 2006

**HAL** is a multi-disciplinary open access archive for the deposit and dissemination of scientific research documents, whether they are published or not. The documents may come from teaching and research institutions in France or abroad, or from public or private research centers.

L'archive ouverte pluridisciplinaire **HAL**, est destinée au dépôt et à la diffusion de documents scientifiques de niveau recherche, publiés ou non, émanant des établissements d'enseignement et de recherche français ou étrangers, des laboratoires publics ou privés.

# Miscible displacement fronts of shear thinning fluids inside rough fractures.

A. Boschan<sup>1,2</sup>, H. Auradou,<sup>1</sup> I. Ippolito,<sup>2</sup> R. Chertcoff,<sup>2</sup> and J.P. Hulin<sup>1</sup>

**Abstract.** The miscible displacement of a shear-thinning fluid by another of same rheological properties is studied experimentally in a transparent fracture by an optical technique imaging relative concentration distributions. The fracture walls have complementary self-affine geometries and are shifted laterally in the direction perpendicular to the mean flow velocity  $\mathbf{U}$  : the flow field is strongly channelized and macro dispersion controls the front structure for Péclet numbers above a few units. The global front width increases then linearly with time and reflects the velocity distribution between the different channels. In contrast, at the local scale, front spreading is similar to Taylor dispersion between plane parallel surfaces. Both dispersion mechanisms depend strongly on the fluid rheology which shifts from Newtonian to shear-thinning when the flow rate increases. In the latter domain, increasing the concentration enhances the global front width but reduces both Taylor dispersion (due to the flattening of the velocity profile in the gap of the fracture) and the size of medium scale front structures.

## 1. Introduction

The transport of dissolved species in fractured formations is of primary importance in a large number of groundwater systems : predicting the migration rate and the dispersion of contaminants from a source inside or at the surface of a fractured rock is then relevant to many fields such as waste storage and water management (*National Research Council* [1996]; *Adler and Thovert* [1999]; *Berkowitz* [2002]).

In the present work, these phenomena are studied experimentally by analyzing relative concentration distributions during the displacement of a transparent fluid by a miscible dyed one inside a model transparent rough fracture. A key characteristic of these fractures is the self-affine geometry of their wall surfaces : it reproduces the multiscale geometrical characteristics of many faults and “fresh” fractures. For such surfaces, the variance  $\Delta h^2 = \langle (h(\vec{r} + \Delta\vec{r}) - h(\vec{r}))^2 \rangle$  of the local height  $h(x, y)$  of the surface with respect to a reference plane verifies :

$$\frac{\Delta h}{l} = \left(\frac{\Delta r}{l}\right)^\zeta, \quad (1)$$

in which  $(x, y)$  are coordinates in the plane of the fracture,  $\zeta$  is the self-affine exponent,  $l$  the topothesy (i.e. the length scale at which the slope  $\Delta h/\Delta r$  is of the order of 1).

In this work, the rough fracture walls have complementary geometries : they are separated by a small distance normal to their mean plane and shifted laterally relative to each other. This shear displacement induces local aperture variations : experimental and numerical investigations demonstrate that, in this case, preferential flow paths dominantly perpendicular to the shear appear (*Gentier et al.*

[1997]; *Yeo et al.* [1998]; *Auradou et al.* [2005]). These paths strongly influence fluid transport (*Neretnieks et al.* [1982]; *Tsang and Tsang* [1987]; *Brown et al.* [1998]; *Becker and Shapiro* [2000]), particularly when the mean flow is, as here, parallel to these channels.

The objective of the present paper is to study the influence of the structures of the aperture field on the displacement front of a transparent fluid by a dyed miscible one. For that purpose, the displacement process is studied at different length scales in order to identify the different front spreading mechanisms. Practically, the displacement front is analyzed in regions of interest of variable widths  $W$  perpendicular to the flow. If  $W$  is smaller than the local fracture aperture, the front spreading will be dispersive and controlled by local mechanisms; for large  $W$  values of the order of transverse size of the fracture (100 times the aperture) the front structure is controlled, on the contrary, by preferential flow paths. Additional informations on these mechanisms will be obtained from the influence of the flow velocity and of the rheology of the fluids.

## 2. Dispersion and front spreading in rough fractures

Previous studies by *Ippolito et al.* [1993]; *Roux et al.* [1998]; *Adler and Thovert* [1999]; *Detwiler et al.* [2000] described mixing in fractures by a Gaussian convection-dispersion equation. They suggested that the dispersion coefficient is the sum of the contributions of geometrical and Taylor dispersion. The latter results from the local advection velocity gradient between the walls of the fracture : its influence is balanced by molecular diffusion across the gap. There results a macroscopic Fickian dispersion parallel to the flow (*Taylor* [1951]; *Aris* [1958]) characterized by the coefficient :

$$\frac{D}{D_m} = \tau + f Pe^2, \quad (2)$$

where  $D_m$  is the molecular diffusion coefficient, the Péclet number  $Pe = Ua_0/D_m$  represents the relative influence of the velocity gradients and molecular diffusion,  $U$  the average flow velocity in the whole fracture,  $a$  the gap thickness,  $\tau$  the tortuosity of the void space reducing the rate of longitudinal molecular diffusion (*Bear* [1972]; *Drazer and Koplík* [2002]); for flat parallel plates and a Newtonian fluid,  $f = 1/210$ .

<sup>1</sup>Laboratoire Fluides, Automatique et Systèmes Thermiques, UMR No. 7608, CNRS, Université Paris 6 and 11, Bâtiment 502, Université Paris Sud, 91405 Orsay Cedex, France.

<sup>2</sup>Grupo de Medios Porosos, Facultad de Ingeniería, Universidad de Buenos Aires, Paseo Colón 850, 1063 Buenos-Aires, Argentina.

Geometrical dispersion reflects the disorder of the velocity field in the fracture plane and may be significant in rough fractures. Theoretical investigations by *Roux et al.* [1998] suggest that this geometrical mechanism is important at intermediate  $Pe$  values; at lower (resp. higher) Péclet numbers, molecular diffusion (resp. Taylor dispersion) are dominant. Scaling arguments allow in addition to estimate Péclet numbers corresponding to the limits of these domains : they depend on the mean, the variance and the correlation length of the aperture field. Such predictions are supported by experimental investigations on model fractures with a relatively weak disorder of the aperture field (*Ippolito et al.* [1993, 1994]; *Adler and Thovert* [1999]; *Detwiler et al.* [2000]).

In natural fractures, however, experimental (*Neretnieks et al.* [1982]; *Brown et al.* [1998]; *Becker and Shapiro* [2000]) and numerical (*Drazer et al.* [2004]) studies indicate that mass transport is strongly influenced by large scale preferential flow channels parallel to the mean velocity. Anomalous dispersion is then expected as in the analogous case of porous media with strata of different permeabilities (*Mathéron and de Marsily* [1980]). As pointed out by (*Roux et al.* [1998]), similar effects are expected in fracture if the flow velocities vary more slowly along a streamline than perpendicular to it. Then, large distortions of the displacement front (*Drazer et al.* [2004]) may appear and grow linearly with time. Moreover, in highly distorted parts of the front, transverse concentration gradients appear and induce a transverse tracer flux that further enhances dispersion.

Another important parameter influencing miscible displacements is the rheology of the flowing fluids (relevant, for instance, to enhanced oil recovery using polymer solutions (*Bird, Armstrong and Hassager* [1987])). Non linear rheological properties modify indeed the flow velocity field and, more specifically, the flow velocity contrasts (*Shah and Yortsos* [1995]; *Fadili et al.* [2002]). In the case of shear-thinning fluids in simple geometries like tubes or parallel plates, the flow profile is no longer parabolic but flattens in the center part of the flow channels where the shear rate is lowest : this decreases the dispersion coefficient (compared to the Newtonian case) but the square law variation of the dispersion coefficient with the Peclet number is still satisfied. For instance, when the viscosity  $\mu$  varies with the shear rate  $\dot{\gamma}$  following a power law :  $\mu \propto \dot{\gamma}^{n-1}$ , Eq. 2 remains valid but  $f$  is a function of  $n$  (*Vartuli et al.* [1995]).

In heterogeneous media, on the contrary, numerical investigations suggest that the flow of shear thinning fluids gets concentrated in a smaller number of preferential flow paths than for Newtonian ones (*Shah and Yortsos* [1995]; *Fadili et al.* [2002]): the macrodispersion reflecting large scale distortions of the displacement front is then increased (even though the local dispersion due to the flow profile in individual channels is still reduced). Finally, in this work and in contrast with oil recovery, the polymer concentration in the injected and displaced fluids is the same : we investigate only its influence on the transport of a passive solute. The influence of the shear thinning properties is studied by running experiments with different polymer concentrations.

### 3. Experimental set-up and procedure

#### 3.1. Model fractures and fluid injection set-up

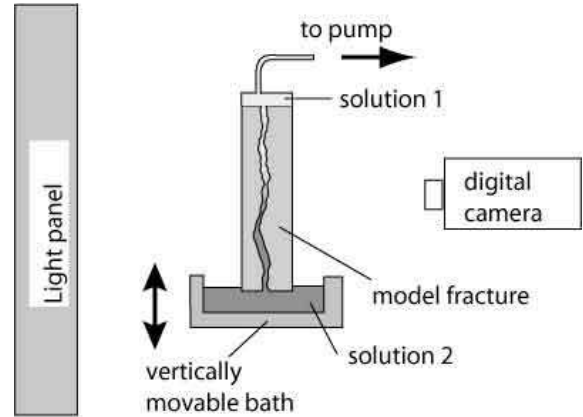


Figure 1. Schematic view of the experimental setup.

Model fractures used in the present work are made of two complementary transparent rough self-affine surfaces clamped together. A self-affine surface is first generated numerically using the mid-point algorithm (*Feder* [1988]) with a self-affine exponent  $\zeta$  equal to the value 0.8 measured for many materials, including granite (*Bouchaud* [2003]). Then, the surfaces are carved by a computer controlled milling machine into a parallelepipedic plexiglas block. The final steps of the machining require a hemispherical tool with a  $600 \mu\text{m}$  diameter. The effective size of the surface is  $171$  by  $85 \text{ mm}$  and the difference in height between the lowest and highest points of the surface is  $19.2 \text{ mm}$  while the mean square deviation of the height is  $3 \text{ mm}$ . The two surfaces are exactly complementary but for a  $0.33 \text{ mm}$  relative shift parallel to their length; they are bounded on their larger sides by  $10 \text{ mm}$  wide borders rising slightly above the surfaces. The geometries of these borders is chosen so that they match perfectly and act as spacers leaving an average mean distance  $a_0 = 0.75 \text{ mm}$  between the surfaces when the blocks are clamped together. In all cases, the gap between the surfaces is large enough so that the two walls do not touch : both the mean aperture  $a_0$  and the relative displacement are the same in all experiments.

The fracture assembly is positioned vertically (Fig. 1) with the two vertical sides (corresponding to the borders) sealed while the two others are open. The upper side of the model is connected to a syringe pump sucking the fluids upwards out of the fracture. The lower horizontal side is dipped into a reservoir which may be moved up and down. The fracture is first saturated by sucking fluid out of the lower reservoir into the model. Then, the original fluid is replaced by the other after lowering the reservoir before raising it again and starting the displacement experiment by pumping fluid at the top of the model. This procedure avoids unwanted intrusions while replacing a fluid by the other and allows to purge completely the lower reservoir; a perfectly straight front between the injected and displaced fluids is obtained in this way at the onset of the experiment.

#### 3.2. Fluid preparation and characteristics

In all experiments, the injected and displaced fluids are identical water-scleroglucan solutions but for a small amount of Water Blue dye (*Handbook of dyes* [2002]) added to one of the solutions at a concentration  $c_0 = 0.3 \text{ g/l}$ .  $\text{NaCl}$  is added to the other solution to keep both densities equal. The dye has been chosen such that it has no physico-chemical interaction with the model walls and can be considered as a

passive tracer. The molecular diffusion coefficient of the dye  $D_m \simeq 6.5 \times 10^{-10} \text{ m}^2 \cdot \text{s}^{-1}$  is determined independently from Taylor dispersion measurements in a capillary tube.

The rheological properties of the scleroglucan solutions have been characterized using a *Contraves LS30* Couette rheometer in range of shear rates  $0.016 \text{ s}^{-1} \leq \dot{\gamma} \leq 87 \text{ s}^{-1}$ . The rheological properties of the solutions have been verified to be constant with time within experimental error (over a time lapse of 3 days) and to be identical for the dyed and transparent solutions (for a same polymer concentrations). The variation of the viscosity  $\eta$  with  $\dot{\gamma}$  is well fitted by the classical Carreau formula :

$$\eta = \frac{\eta_0 - \eta_\infty}{(1 + (\frac{\dot{\gamma}}{\dot{\gamma}_0})^2)^{\frac{1-n}{2}}} + \eta_\infty. \quad (3)$$

The values of these rheological parameters for the polymer solutions used in the present work are listed in Table 1.  $\eta_\infty$  is taken equal to the value of the solvent viscosity ( $10^{-3} \text{ Pa}\cdot\text{s}$  for water) since its determination would require measurements beyond the experimental range limited to  $\dot{\gamma} = 87 \text{ s}^{-1}$ . In Eq.(3),  $\dot{\gamma}_0$  corresponds to a crossover between two regimes. For  $\dot{\gamma} < \dot{\gamma}_0$ , the viscosity  $\eta$  tends to  $\eta_0$ , and the fluid behaves as a newtonian fluid. On the other hand, for  $\dot{\gamma} > \dot{\gamma}_0$ ,  $\eta$  decreases following a power law  $\mu \propto \dot{\gamma}^{(n-1)}$ . Note that, due to the small volume fraction of polymer, the molecular diffusion coefficient keeps the same value as in pure water.

**Table 1.** Rheological parameters of scleroglucan solutions used in the flow experiments.

Polymer Conc. ppm	$n$	$\dot{\gamma}_0$ $\text{s}^{-1}$	$\eta_0$ $\text{mPa}\cdot\text{s}$
500	$0.38 \pm 0.04$	$0.077 \pm 0.018$	$410 \pm 33$
1000	$0.26 \pm 0.02$	$0.026 \pm 0.004$	$4490 \pm 342$

### 3.3. Optical relative concentration measurements

The flow rate is kept constant during each experiment and ranges between 0.01 and 1 *ml/min*. The total duration of the experiments in order to obtain a complete saturation of the fracture by the invading fluid varies between 20 *min* and 33 *hours*. The transparent fracture is back illuminated by a light panel : about 100 images of the distribution of light transmitted through the fracture are recorded at constant intervals during the fluid displacement using a Roper Coolsnap HQ digital camera with a high, 12 bits, dynamic range. Reference images are recorded both before the experiments and after the full saturation by the displacing fluid in order to have images corresponding to the fracture fully saturated with both the transparent and the dyed fluid.

The local relative concentration of the displacing fluid (averaged over the fracture aperture) is determined from these images by the following procedure. First, the absorbance  $A(x, y, t)$  of light by the dye on an image obtained at the time  $t$  is computed by the relation :

$$A(x, y, t) = \ln\left(\frac{I_t(x, y)}{I(x, y, t)}\right) \quad (4)$$

in which  $I_t(x, y)$  and  $I(x, y, t)$  are the transmitted light intensities (in grey levels) measured for a pixel of coordinates  $(x, y)$  respectively when the fracture is saturated with transparent fluid and at time  $t$ . When the fracture is saturated with the dyed fluid ( $c(x, y) = c_0$ ), the transmitted light intensity is  $I_0(x, y)$  so that the adsorbance  $A_0(x, y)$  is :

$$A_0(x, y) = \ln\left(\frac{I_t(x, y)}{I_0(x, y)}\right) \quad (5)$$

The relation between the local concentration  $c(x, y, t)$  (averaged over the local fracture aperture), the dye concentration  $c_0$  in the dyed fluid and the absorbances  $A$  and  $A_0$  has been determined independently from calibration pictures realized with the fracture saturated with dyed solutions of concentrations  $c$  increasing from 0.1 to 0.5 *g/l*. The ratio  $A(x, y)/A_0(x, y)$  is found experimentally to be constant within  $\pm 3\%$  over the picture area : for more precision, the ratio  $\langle A \rangle_{x,y} / \langle A_0 \rangle_{x,y}$  of the averages is therefore used to determine the calibration curve. Due to non linear adsorbance (*Detwiler et al.* [2000]), the relation  $c/c_0 = \langle A \rangle_{x,y} / \langle A_0 \rangle_{x,y}$  predicted by Beer-Lambert's law is not valid. The variation of  $c/c_0$  with  $\langle A \rangle / \langle A_0 \rangle$  follows however accurately the polynomial relation :

$$\frac{c}{c_0} = b_1 \frac{A}{A_0} + b_2 \left(\frac{A}{A_0}\right)^2 + b_3 \left(\frac{A}{A_0}\right)^3 \quad (6)$$

with  $b_1 = 0.186 \pm 0.023$ ,  $b_2 = 0.0087 \pm 0.04$  and  $b_3 = 0.108 \pm 0.021$ . Practically, Eq. 6 is applied to all pixels  $(x, y)$  in the pictures recorded during the experiment in order to obtain  $c(x, y, t)/c_0$ . An instantaneous relative concentration map obtained in this way is displayed in Fig. 2.

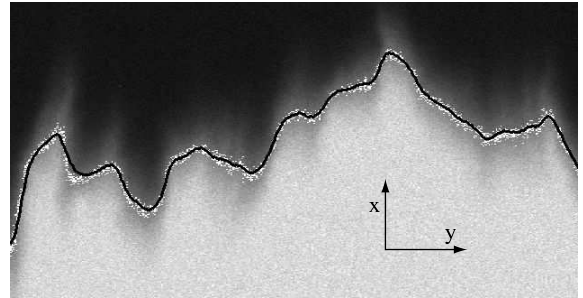


**Figure 2.** Experimental relative concentration field obtained with a 1000 *ppm* polymer concentration for a mean front displacement of half the fracture length. Grey levels represent values of the ratio  $c(x, y, t)/c_0$ . Size of field of view : 81 *mm*  $\times$  70 *mm*; only a part of the actual image is shown. Solid line : front profile  $x_f(y, t)$  as defined in section 6.1; white dots are pixels where  $c(x, y, t)/c_0 = 0.5 \pm 0.03$ .

In the following,  $c_0$  is omitted and  $c(x, y, t)$  refers to the local *relative* concentration at a given time (still averaged as above over the fracture aperture).

## 4. Local concentration variations

As already pointed above, transport in the fracture results from the combination of front spreading due to large scale flow velocity variations and of mixing due to local dispersion mechanisms and concentration gradients. In order to identify these different processes, a local analysis is first performed.

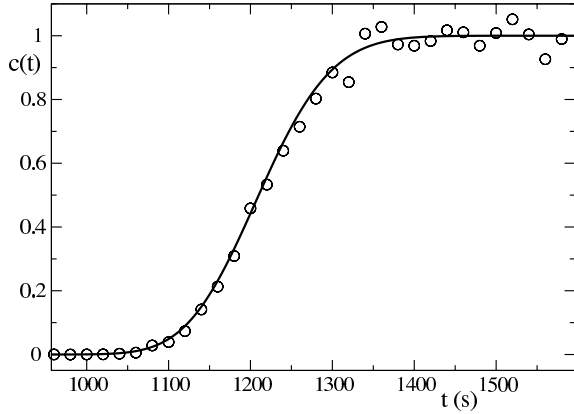


**Figure 3.** Time variation of the relative concentration  $c(x, y, t)$  for  $x = 20 \text{ mm}$  and  $y = 36 \text{ mm}$  for 1000 ppm polymer solutions. Mean flow velocity  $U = 0.014 \text{ mm/s}$  ( $Pe = 150$ ). Solid line : fit by Eq.7 with  $\overline{t(x, y)} = 1212 \text{ s}$  and  $D(x, y) = 0.315 \text{ mm}^2/\text{s}$ .

For each pixel  $(x, y)$ , the variation  $c(x, y, t)$  with time of the local relative concentration of the dyed fluid has been determined; as can be seen in Fig. 3, it is well fitted by the following solution of the convection-dispersion equation corresponding to the stepwise concentration variations induced experimentally :

$$c(x, y) = \frac{1}{2} \left( 1 + \operatorname{erf} \frac{t - \overline{t(x, y)}}{\sqrt{4 \frac{D(x, y)}{U^2} t}} \right) \quad (7)$$

In Eq. 7,  $U$  is the mean velocity,  $D(x, y)$  is the local dispersion coefficient and  $\overline{t(x, y)}$  the mean transit time. Note that, if the injected fluid is the transparent one, the + sign should be replaced by a - in Eq. 7. Both  $D(x, y)$  and  $\overline{t(x, y)}$  are defined locally and may depend on the measurement point.

In the following, the variations of these quantities are analyzed : on the one hand, the spatial variations of  $\overline{t(x, y)}$  reveal the channelized structure of the flow that leads to macrodispersion. On the other hand,  $D(x, y)$  reflects local mixing processes taking place on each flow line.

## 5. Local dispersive mixing

In this section, the variation of  $D(x, y)$  is studied as a function of the distance  $x$  from the inlet and of the fluid velocity and rheology. The probability distribution of the local values of  $D(x, y)$  determined for all pixels at a same distance  $x$  for a given experiment is displayed in Fig. 4a in a grey level scale as a function of  $x$  ( $45 \leq x \leq 125 \text{ mm}$ ); Fig. 4b shows the two extreme distributions corresponding to  $x = 45$  (solid line) and  $125 \text{ mm}$ . One observes that the mean value  $\overline{D}$  of the distributions increases only by 20% between  $x = 45$  and  $125 \text{ mm}$ .  $\overline{D}$  will just be referred to as  $D$  in the following and the deviations of the local values will be characterized by the width  $\Delta D$  of  $P(D)$  at mid-height which increases also slowly with distance). The drift of  $D$  may be due to slow variations of the mean aperture and flow velocity. It may also reflect an increased dispersion in distorted regions of the front : there, dye diffuses across the flow lines which contributes to broaden the front. The slow variation of the mean value of  $D$  with  $x$  together with the good fit displayed in Fig. 3, demonstrate that the Fickian dispersion model describes well the local spreading of the front during all the experiment . The symmetry of the process is finally checked by realizing the same experiments with the transparent solution displacing the dyed one. The distributions of the dispersion coefficients for given values of  $x$  are the

same as in the reverse configuration : there is therefore no effect of small residual density contrasts..

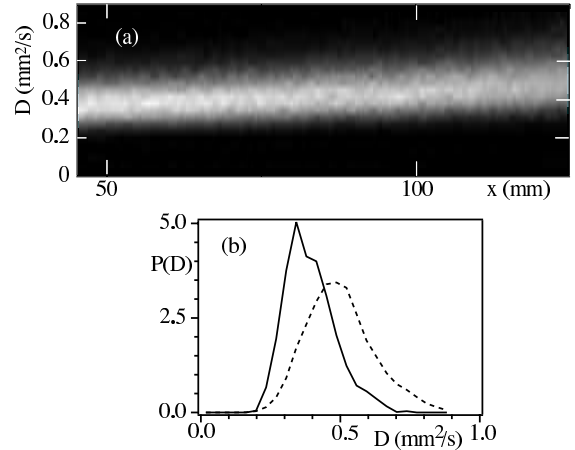


**Figure 4.** Probability distribution  $P(D, x)$  of the dispersion coefficient for a dyed solution displacing a transparent one : mean flow velocity  $U = 0.014 \text{ mm/s}$  ( $Pe = 150$ ), polymer concentration 1000 ppm). - (a) Grey levels correspond to the value of the probability  $P(D)$  at the corresponding values of  $D$  and  $x$  - (b) Distributions  $P(D)$  respectively for  $x = 45$  (solid line) and  $125 \text{ mm}$  (dashed line).

The dependence of the local dispersion on the flow velocity  $U$  for the 500 ppm and 1000 ppm solutions is displayed in figure 5 where  $D$  is plotted as a function of the Péclet number  $Pe$  defined above. The same variation trends are followed for both solutions : for low  $Pe$  values the dispersion coefficient tends towards a constant close to 1, while at high  $Pe$ ,  $D$  increases as the square of  $Pe$ . These variations are similar to the predictions of Eq. 2 (solid, dotted and dashed lines) also plotted in figure 5 for a newtonian fluid and two power law shear thinning fluids for which  $\mu \propto \dot{\gamma}^{n-1}$  ( $n$  is taken equal to the values listed in Tab. 1 and the value of  $f$  in Eq.2 is computed from Eq. 4 in *Boschan et al* [2003]). The overall agreement observed implies that Taylor dispersion is indeed the dominant mechanism controlling local dispersion.

In a more detailed analysis, one must however take into account the fact that, for real fluids, the viscosity does not diverge at low shear rates but becomes constant (Newtonian plateau viscosity) for  $\dot{\gamma} < \dot{\gamma}_0$ . In a Poiseuille Newtonian flow between two parallel flat plates, the shear rate is maximum at the wall with  $\dot{\gamma} = 6U/a$ . It follows that the transition value  $\dot{\gamma}_0$  is reached for  $U = U_c = a\dot{\gamma}_0/6$ . Using the values of  $\dot{\gamma}_0$  in Tab.1, the velocities  $U_c$  (resp. Péclet numbers  $Pe_c$ ) corresponding to the 500 ppm and 1000 ppm solutions are  $0.01 \text{ mm/s}$  and  $0.003 \text{ mm/s}$  (resp.  $Pe_c = 11$  and 4). Below  $Pe_c$ , the dispersion coefficient should be the same as for a Newtonian fluid; above  $Pe_c$ , its variation should progressively merge with that predicted for power law fluids. This crossover is clearly observed in Fig.5 : for  $Pe < 30$ , values of  $D$  obtained with the 500 ppm and 1000 ppm solutions coincide with the predictions for Newtonian fluids. At high Péclet numbers, data points corresponding to the two solutions get separated and the values of  $D$  become close to the predictions for power law fluids with the corresponding values of  $n$ .

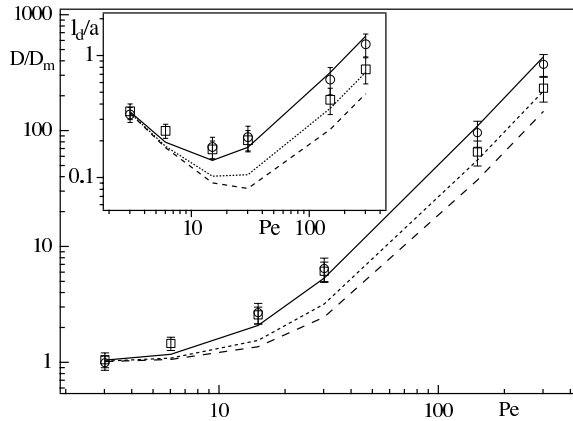


**Figure 5.** Variation of normalized dispersion coefficient  $D/D_m$  with  $Pe = Ua_0/D_m$ . Insert : variation of the dispersivity  $l_d = D/U$ . Solid, dotted and dashed lines : predictions from Eq. 2 respectively for  $n = 1$  (Newtonian fluid),  $n = 0.38$  and  $n = 0.26$  (shear thinning solutions with respective 500 ppm and 1000 ppm polymer concentrations).

It is often convenient to replace the dispersion coefficient  $D$  by the dispersivity  $l_d = D/U$  to identify more easily the influence of spatial heterogeneities of the flow field. For Taylor like dispersion verifying Eq.2 and for a Newtonian fluid, the dispersivity has a minimum equal to  $l_d = 2a/\sqrt{210} \approx 0.0095a$  for  $Pe = \sqrt{210} \simeq 14.5$ . The insert of Fig.5 displays the variation of the dispersivity with  $Pe$  : its minimum value corresponds well to the theoretical prediction for Newtonian fluids (solid line). This confirms that, in this range of Péclet numbers, the two polymer solutions behave like Newtonian fluids.

These results demonstrate that the local dispersion  $D(x, y)$  in the rough model fracture is mainly due to the flow profile in the gap between the walls and similar to that between flat parallel plates. This is likely due to two properties of the flow field : first, as for parallel plates, flow lines initially located in the center of the gap remain there during their full path through the fracture and, similarly, those located close to a wall only move away from it through molecular diffusion. Also, the orientation of the local flow velocity is always close to that of the mean flow as will be seen below. In the next section, we discuss on the contrary macrodispersion due to variations in the plane of the fracture of the local velocities (averaged this time over the gap).

## 6. Macrodispersion in the model fractures

### 6.1. Flow structure and mean front profile

As pointed above, the complementary rough walls of the fracture model are translated relative to each other in the direction  $y$  perpendicular to the mean flow (along the  $x$  axis) : in this configuration, large scale channels parallel to  $x$  appear (Gentier et al. [1997]; Drazer et al. [2004]; Auradou et al. [2005]) with only weak variations of the flow velocity along their length (Auradou et al. [2006]). In the following, we use a simple model in which the fracture is described as a

set of independent parallel channels where the effective flow velocity  $U(y)$  depends only on the transverse coordinate.



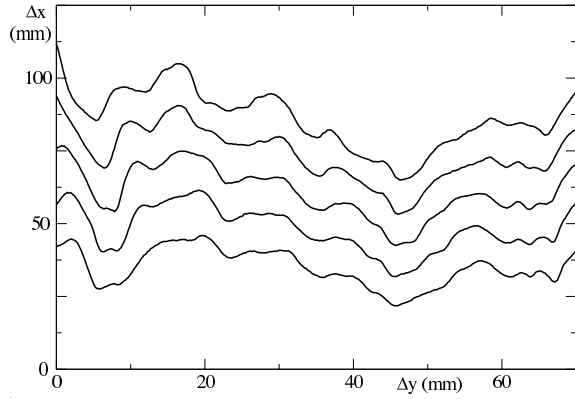
**Figure 6.** Greyscale map of the normalized local transit time  $\bar{t}(x, y)U/x$ . Flow is from left to right. Dark (resp. light) regions correspond to locations where  $\bar{t}(x, y)U/x < 1$  (resp.  $\bar{t}(x, y)U/x > 1$ ). Mean flow velocity  $U = 0.014 \text{ mm/s}$  ( $Pe = 150$ ), polymer concentration 1000 ppm).

The validity of this assumption is tested in Fig. 6 in which the values of the normalized transit time  $\bar{t}(x, y)U/x$  are represented as grey levels at all points  $(x, y)$  inside the field of view;  $\bar{t}(x, y)$  is the local effective transit time determined by fitting the curve of Fig. 3 corresponding to point  $(x, y)$  by solutions of Eq. 7. Dark (resp. light) pixels mark points where  $\bar{t}(x, y)U/x$  is respectively higher (resp. lower) than 1 : dark and light streaks globally parallel to  $x$  are clearly visible and extend over the full length of the model fractures. These streaks correspond to slow (resp. fast) flow paths and their orientation deviates only slightly from  $x$  : this is in agreement with the above simple model of parallel flow paths with different velocities remaining correlated along the full path length.

Another important feature of the maps of Fig. 6 is that they allow to determine an instantaneous front profile  $x_f(y, t)$  at a given time  $t$  : in the following, it will be defined as the set of all points for which  $\bar{t}(x, y) = t$ . In our experiments this profile was very similar to the isoconcentration line  $c(x, y, t)/c_0 = 0.5$  (as can be seen in Fig. 2). In the following, the macrodispersion process will be directly characterized by the variations of these front profiles with time without analyzing extensively the concentration maps.

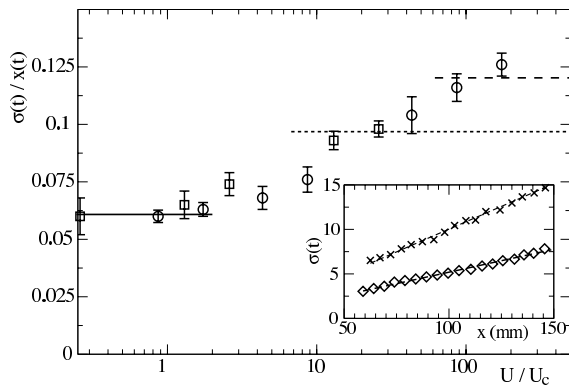
### 6.2. Global front dynamics

Fig.7 displays several front profiles obtained at different times by this procedure. As expected, the profile is initially quite flat but large structures appear and grow with time. A key feature is the fact that similar structures are observed on all fronts : it is only their size parallel to the mean flow that increases with time. This confirms the large correlation length parallel to  $x$  of the high and low velocity regions and, therefore, the flow channelization already assumed above.



**Figure 7.** Front profiles  $x_f(y, t)$  at times  $t = 6.5, 8, 9.5, 11$  and  $12.5 \text{ min}$  for a  $1000 \text{ ppm}$  polymer solution and  $U = 0.014 \text{ mm/s}$  ( $Pe = 150$ ) The mean flow velocity is oriented from the bottom to the top of the figure).

In such cases, as pointed out by *Drazer et al.* [2004], the size of the structures of the front, and therefore its global width  $\sigma(t)$  should increase linearly with distance (and time). In the following, the width  $\sigma(t)$  is defined by  $\sigma^2(t) = \langle (x_f(y, t) - \langle x_f(y, t) \rangle_y)^2 \rangle_y$  in which  $\langle x_f(y, t) \rangle_y$  is the mean distance of the front from the inlet at time  $t$ : as shown in the insert of Fig.8,  $\sigma(t)$  increases as expected linearly with time.



**Figure 8.** Variation in Log linear coordinates of the relative front width  $\sigma(t)/x(t)$  with the normalized mean velocity  $U/U_c$ ; crossover velocity  $U_c = 0.01 \text{ mm/s}$  (resp.  $0.003 \text{ mm/s}$ ) for ( $\square$ ):  $500 \text{ ppm}$  (resp. ( $\circ$ )  $1000 \text{ ppm}$ ) solutions. Solid, dotted and dashed horizontal lines: predicted values respectively for a Newtonian fluid and power law fluids with same index  $n$  as the  $500 \text{ ppm}$  and  $1000 \text{ ppm}$  solutions. Insert: variation of  $\sigma(t)$  ( $\text{mm}$ ) with the distance  $x$  for a  $1000 \text{ ppm}$  solution. Diamonds:  $U = 0.0056 \text{ mm/s}$  ( $Pe = 60$ ), Crosses:  $U = 0.056 \text{ mm/s}$  ( $Pe = 600$ ). Dashed line: linear regression.

Since the mean distance  $\langle x_f(y, t) \rangle_y$  also increases linearly with time, the ratio  $\sigma(t)/\langle x_f(y, t) \rangle_y$  remains constant and may therefore be used to characterize the magnitude of the macrodispersion. In the framework of the simple model assuming parallel independent channels with different flow velocities,  $\sigma(t)$  and  $\langle x_f(y, t) \rangle_y$  are respectively of the order of  $\delta U t$  and  $U t$  where  $\delta U$  the root mean square of the velocity variations between the different channels. Therefore, the ratio  $\sigma(t)/\langle x_f(y, t) \rangle_y$  corresponds to the relative magnitude  $\delta U/U$  of the velocity contrasts inside the

fracture (a well known result for stratified media with negligible exchange between layers).

For both Newtonian ( $\eta = \text{cst.}$ ) and power law ( $\eta \propto \dot{\gamma}^{n-1}$ ) fluids the relative velocity fluctuations  $\delta U \propto U$  are expected to be constant with  $U$ :  $\sigma(t)/x(t)$  should therefore be independent of the flow rate  $Q$ . The variations of  $\sigma(t)/x(t)$  with the normalized velocity  $U/U_c$  for the two polymer solutions used in our experiments are displayed in Fig.8 ( $U_c$  is the cross-over velocity between the Newtonian and shear thinning behaviours introduced in section. 5), The values of  $\sigma(t)/x(t)$  are averages over several time intervals (error bars indicate fluctuations with time). For  $U < U_c$ ,  $\sigma(t)/x(t)$  retains a constant value close to 0.05 independent of the polymer concentration which likely corresponds to a Newtonian behaviour. For  $U > U_c$ ,  $\sigma(t)/x(t)$  increases faster with  $U$  for the more concentrated ( $1000 \text{ ppm}$ ) solution. The normalized widths should reach a new limit at higher flow rates ( $U \gg U_c$ ): theoretical values for the two solutions are indicated as horizontal lines.

More precisely, the shear rate  $\dot{\gamma}$  is always zero in the middle of the gap of the fracture and highest at the walls. If the shear rate at the wall is larger than the transition value  $\dot{\gamma}_0$  (see section 5), there are two domains in the velocity profile: the fluid rheology is Newtonian in the central part of the fracture and non Newtonian near the walls (*Gabbanelli et al.* [2005]). When the flow rate  $Q$  increases, the fraction of the flow section where flow is Newtonian shrinks while the fraction where it is non Newtonian expands: for a shear thinning fluid with a power law characteristic ( $n < 1$ ), the average velocity in a given flow channel (the integral of the velocity profile over the fracture gap) increases faster with the longitudinal pressure gradient (as  $\nabla p^{1/n}$ ) than for Newtonian fluids (as  $\nabla p$ ). This enhances velocity contrasts between channels of different apertures (assuming that they are subject to similar pressure gradients) and finally increases the front width compared to the Newtonian case. These effects get larger as the concentration increases from  $500$  to  $1000 \text{ ppm}$  both because the exponent  $n$  decreases and because the transition shear rate  $\dot{\gamma}_c$  is smaller (Tab. 1). This lower value of  $\dot{\gamma}_c$  for the  $1000 \text{ ppm}$  solution does indeed increase the fraction of the flow section where the fluid rheology is shear thinning.

### 6.3. Front geometry

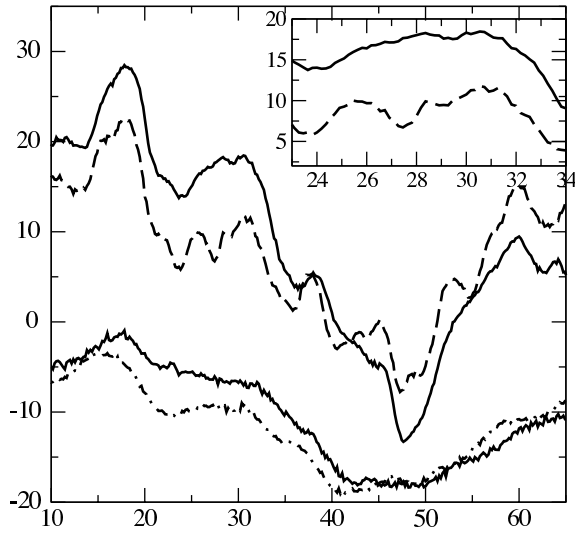


**Figure 9.** Front geometries for a mean distance from the inlet equal to half the fracture length. Solid (resp. dashed) lines : 1000 ppm (resp. 500 ppm) solutions. Top (resp. bottom) curves :  $U = 0.3 \text{ mm/s}$  i.e.  $Pe = 3000$  (resp.  $U = 0.003 \text{ mm/s}$  i.e.  $Pe = 30$ ). The two sets of curves have been shifted to allow for easier comparisons. Insert : close up of the upper curves ( $U = 0.3 \text{ mm/s}$  i.e.  $Pe = 3000$ ).

In the previous section, the overall front width has been shown to depend on the global flow rate and on the fluid rheology; their influence on the detailed front structure will now be analyzed. Figure 9 compares front geometries observed for the two solutions used in the experiments at the lowest (resp. highest) mean velocities investigated :  $U = 0.003 \text{ mm/s}$  (resp.  $0.3 \text{ mm/s}$ ). The lower velocity is below  $U_c$  and the rheology of both fluids is therefore Newtonian. The polymer concentration plays then a minor part and the front geometries are very similar (lower curves). In addition, at this mean velocity, the Péclet number is  $\approx 3$  and therefore lower than the value  $Pe \approx 14.5$  (see section 5) corresponding to the crossover between Taylor dispersion and longitudinal molecular diffusion. As a result, transport at the local scale is controlled by molecular diffusion which smears out the effect of local velocity fluctuations and smoothens the front geometry.

The higher velocity  $U = 0.3 \text{ mm/s}$  (upper curves) is well above  $U_c$  : the global front width increases then with the polymer concentration (see section 6.2), as can be seen for the two upper curves in Fig.9. However, at smaller length scales, the geometrical characteristics of the front and their dependence on the fluid rheology are more complex. Geometrical features of lateral size below  $10 \text{ mm}$  have, for in-

stance, a larger extension parallel to the mean flow for the  $500 \text{ ppm}$  solution.

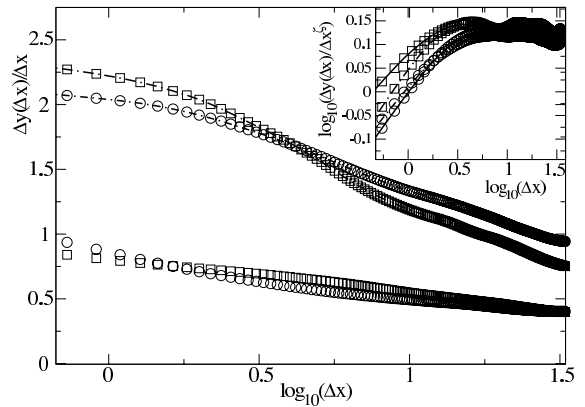


**Figure 10.** Variation of the ratio  $\Delta y(\Delta x)/\Delta x$  as a function of  $\log_{10}(\Delta x)$  for the same fronts as in Fig. 9 with  $\circ$  (resp.  $\square$ ) : 1000 ppm (resp. 500 ppm) polymer solutions. Symbols with no lines :  $U = 0.003 \text{ mm/s}$  ( $Pe = 30$ ) and with dotted lines :  $U = 0.3 \text{ mm/s}$  ( $Pe = 3000$ ). Insert : variation of  $\log_{10}(\Delta y/\Delta x^{\zeta_f})$  as a function of  $\log_{10}(\Delta x)$  ( $\zeta_f$  has been chosen equal to 0.8 in order to provide the best fit with a power law at large  $\Delta x$  values).

Previous theoretical, experimental and numerical studies of displacement fronts between sheared complementary self-affine walls indicate that their geometry is also self-affine (over a finite range of length scales) with the same characteristic exponent  $\zeta$  as the fracture walls (Roux *et al.* [1998]; Drazer *et al.* [2004]; Auradou *et al.* [2001]). Such self-affine profiles  $y(x)$  may be characterized quantitatively from the maximum variation  $y_{max} - y_{min}$  of  $y(x)$  in a window of width  $\Delta x$  ( $y_{max}$  and  $y_{min}$  are the maximum and minimum values of  $y(x)$  in this window). In this "min-max" method, the average  $\Delta y(\Delta x)$  of the values of  $y_{max} - y_{min}$  is computed for all locations of the window inside the profile and the process is repeated for the different values of  $\Delta x$ . For a self-affine curve of characteristic roughness exponent  $\zeta_f$ , one has, for instance,  $\Delta y \propto \Delta x^{\zeta_f}$  ( $\zeta_f = 1$  corresponds to a Euclidian curve).

This result is verified in the insert of Fig.10 where the ratio  $\Delta y/\Delta x^{\zeta_f}$  is plotted as a function of  $\Delta x$  in log-log coordinates for  $\zeta_f = 0.8$  :  $\Delta y/\Delta x^{\zeta_f}$  is indeed observed to remain constant over a broad range of variation of  $\Delta x$  (see insert of Fig. 10). The lower boundary of this self affine domain increases slightly with the polymer concentration from  $\approx 3 \text{ mm}$  (500 ppm) to  $\approx 5 \text{ mm}$  (1000 ppm) and depends weakly on the flow velocity (provided  $Pe \gg 1$ ). For  $\Delta x$  below this cross over length, the slope of the curves is close to 0.2, reflecting an Euclidean geometry with  $\Delta y \propto \Delta x$ .

In order to analyse the influence of the fluid properties and of the flow velocity  $U$  on these results, the variation of the ratio  $\Delta y/\Delta x$  with  $\Delta x$  is displayed in Fig. 10 for the two polymer solutions and for two different values of  $U$  ( $U < U_c$  and  $U > U_c$ ).  $\Delta y$  has been normalised by the window width  $\Delta x$  to reduce the amplitude of the global variations of  $\Delta y$  and make more visible the differences between the curves.

For the lowest velocity  $U$ , the curves are similar for both polymer concentrations (as expected for a Newtonian rheology). The ratio  $\Delta y/\Delta x$  increases with  $U$ , reflecting a higher amplitude of the geometrical features of the front at all length scales : in addition to this global trend, the variation of  $\Delta y$  with  $\Delta x$  depends however significantly on the polymer concentration. For  $U > U_c$  (upper curves in Fig. 10), features of the front with large transverse sizes  $\Delta x$  are of larger



amplitude  $\Delta y$  for the more concentrated solution (as noted above); on the contrary, smaller features corresponding to low  $\Delta x$  values are more developed for the less concentrated solution (this is qualitatively visible on Fig. 9). The two curves cross each other for  $\Delta x \approx 4 \text{ mm}$ . This attenuation of small scale features of the front for the more concentrated solution may reflect an enhancement of the transverse diffusion of the fluid momentum due to its higher viscosity (in other words, drag forces between parallel layers of fluid moving at different velocities become larger). This smoothens out both the local velocity gradients and the associated small features of the front but does not influence large scale velocity variations. These are due to effective aperture contrasts between between parallel channels : their influence is amplified when the exponent  $n$  decreases for higher polymer concentrations, resulting in a larger global front width parallel to the flow.

## 7. Discussion and conclusion

Studying miscible displacement processes by an optical method in a transparent model fracture has revealed important characteristics of flow and transport in rough fractures : these results may be applicable to fluid displacements and transport in fractured reservoirs. A major feature of this approach is the possible simultaneous analysis of both local mixing and global front spreading due to large scale heterogeneities : the different transport mechanisms may in particular be characterized by maps of the local transit time from the inlet and of the local dispersion coefficient.

The multiple length scales features of natural fractures have been reproduced by assuming rough walls of complementary self-affine geometries and with a relative displacement parallel to their mean plane (this models the effect of shear during fracturing). In the present experiments, this relative displacement was perpendicular to the mean flow : this induced a channelization of the flow field with small velocity variations along the flow lines and larger ones across them. Large macrodispersion effects are observed in such a geometry : in the present experiments, the front width increases linearly with distance from the inlet and its structure reflects closely the velocity variations between the different parallel channels.

In contrast, front spreading at the local scale remains diffusive : moreover, the corresponding dispersion coefficient is close to that estimated for Taylor dispersion in an Hele-Shaw cell with plane walls separated by a distance of the order of the main aperture of the fracture. This value may however be locally increased by transverse diffusion in highly distorted regions of the fronts where they get locally parallel to the mean flow.

These fluid displacements are strongly influenced by the rheology of the flowing fluids so that additional informations can be obtained by varying the polymer concentration and/or the shear rate. At low shear-rates (below a transition value  $\dot{\gamma}_0$ ), the polymer solutions used in the present work behave like Newtonian fluids and their concentration has no effect at low mean velocities ( $U < U_c$ ). At higher shear rates ( $U > U_c$ ), the shear thinning effects become significant : they increase with the polymer concentration but may be very different depending on the scale of observation. The global width  $\Delta x$  of the front parallel to the mean flow gets larger at larger polymer concentrations while, in contrast, smaller geometrical features of the front are reduced. In addition, for  $U > U_c$ , polymer also influence at the local scale the Taylor-like dispersion due to the flattening of the flow profile between the fracture walls. Such rheological effects may strongly influence the efficiency of enhanced oil and waste recovery processes.

Such results raise a number of questions to be answered in future work. First, one may expect the spatial correlations of the velocity to decay with distance, leading finally to normal Fickian dispersion. The present samples were not

long enough to allow for the observation of this transition : it may however be more easily observable for models designed so that flow is parallel to the relative shear of the complementary fracture surfaces (in this case, the correlation length should be smaller). Another important issue is the influence of contact area on the transport process : one may expect in this case the development of low velocity regions leading to anomalous dispersion curves.

**Acknowledgments.** We are indebted to G. Chauvin and R. Pidoux for their assistance in the realization of the experimental set-up and to C. Allain for her cooperation and advice. HA and JPH are funded by the EHDRA (European Hot Dry Rock Association) in the frame work of the STREP Pilot plan program SES6-CT-2003-502706) and by the CNRS-PNRH program. This work was also supported by a CNRS-Conicet Collaborative Research Grant (PICS n° 2178) and by the ECOS Sud program n° A03E02.

## References

- Adler, P. M., and J.-F. Thovert (1999), *Fractures and Fracture Networks*, kluwer Academic Publishers, Dordrecht, The Netherlands.
- Aris, R. (1956), On the dispersion of a solute particle in a fluid moving through a tube, *Proceedings of the Royal Society. London. Series A.*, 235, 67–77.
- Auradou, H., J. P. Hulin, and S. Roux (2001), Experimental study of miscible displacement fronts in rough self-affine fractures, *Phys. Rev. E*, 63, 066306.
- Auradou, H., G. Drazer, J. P. Hulin, and J. Koplik (2005), Permeability anisotropy induced by a shear displacement of rough fractured walls, *Water Resour. Res.*, 40, W09423, doi:10.1029/2005WR003938.
- Auradou, H., G. Drazer, A. Boschan, J. P. Hulin, and J. Koplik (2006), Shear displacement induced channelization in a single fracture, *submitted to Geothermics*, available <http://fr.arxiv.org/abs/physics/0603058>.
- Bear, J. (1972), *Dynamics of Fluids in Porous Media.*, American Elsevier, New York. 764p.
- Berkowitz B. (2002), Characterizing flow and transport in fractured geological media : a review, *Advances in water resources*, 25, 861–884.
- Boschan A., V.J. Charette, S. Gabbanelli, I. Ippolito and R. Chertcoff (2003), Tracer dispersion of non-newtonian fluids in a Hele-Shaw cell, *Physica A*, 327, 49–53.
- Becker, M. and A. Shapiro (2000), Tracer transport in fractured crystalline rock: Evidence of nondiffusive breakthrough tailing, *Water Resour. Res.*, 36, 1677–1686.
- Bird R.B., R.C Armstrong and O. Hassager (1987), *Dynamics of polymeric liquids*, vol 1, 2nd editions, Wiley, New-York.
- Bouchaud, E. (2003), The morphology of fracture surfaces: A tool for understanding crack propagation in complex materials, *Surface Review And Letters*, 10, 797–814.
- Brown S., A. Caprihan and R. Hardy, Experimental observation of fluid flow channels in a single fracture, *J. Geophys. Res.*, 103, 5125–5132.
- Detwiler R., H. Rajaram, and R. J. Glass (2000), Solute transport in variable aperture fractures: An investigation of the relative importance of Taylor dispersion and macrodispersion, *Water Resour. Res.*, 36, 1611–1625.
- Drazer, G., and J. Koplik (2002), Transport in rough self-affine fractures, *Phys. Rev. E*, 66, 026303.
- Drazer, G., H. Auradou, J. Koplik, and J. P. Hulin (2004), Self-affine fronts in self-affine fractures: Large and small-scale structure, *Phys. Rev. Lett.*, 92, 014501.
- Fadili A., P. Tardy and A. Pearson (2002), A 3D filtration law for power-law fluids in heterogeneous porous media, *J. Non-Newtonian Fluid Mech.*, 106, 121–146.
- Feder, J. (1988), *Fractals*, Physics of Solids and Liquids, Plenum Press, New York.
- Gabbanelli S., G. Drazer and J. Koplik (2005), Lattice-Boltzmann method for non-newtonian (power law) fluids, *Phys. Rev. E*, 72, 046312.

- Gentier, S., E. Lamontagne, G. Archambault, and J. Riss (1997), Anisotropy of flow in a fracture undergoing shear and its relationship to the direction of shearing and injection pressure, *Int. J. Rock Mech. & Min. Sci.*, 34(3-4), 412.
- Horobin, R.W. and J.A. Kiernan (Eds) (2002), *Conn's Biological Stains: A Handbook of Dyes, Stains and Fluorochromes for Use in Biology and Medicine*, BIOS Scientific Publishers Ltd.
- Ippolito, I., E.J. Hinch, G. Daccord, and J.P. Hulin (1993), Tracer dispersion in 2-D fractures with flat and rough walls in a radial flow geometry, *Phys. Fluids A*, 5(8), 1952-1961.
- Ippolito, I., G. Daccord, E.J. Hinch and J.P. Hulin (1994), Echo tracer dispersion in model fractures with a rectangular geometry, *J. Contaminant Hydrology*, 16(8), 1952-1961.
- Matheron G. and G. de Marsily, (1980), Is transport in porous media always diffusive? A counterexample, *Water Resour. Res.*, 16, 901-917.
- NAS Committee on Fracture Characterization and Fluid Flow (1996), *Rock Fractures and Fluid Flow: Contemporary Understanding and Applications*, National Academy Press, Washington, D.C.
- Neretnieks, I., T. Eriksen, and P. Tahtinen (1982), Tracer movement in a single fissure in granite rock: Some experimental results and their interpretation, *Water Resour. Res.*, 18, 849-858.
- Roux, S., F. Flouraboué, and J. P. Hulin (1998), Tracer dispersion in rough open cracks, *Transport In Porous Media*, 32, 97-116.
- Shah C.B. and Y.C. Yortsos, (1995), Aspects of flow of power-law fluids in porous media, *AIChE Journal*, vol.41(5), 1099-1112.
- Taylor, G.I. (1953), Dispersion of soluble matter in solvent flowing slowly through a tube *Proceedings of the Royal Society. London. Series A.*, 219, 186-203.
- Tsang Y. W., and C.F. Tsang (1987), Channel model of flow through fractured media, *Water Resour. Res.*, vol.23(3), 467-479.
- Vartuli, M., J-P. Hulin and G. Daccord (1995), Taylor dispersion in a polymer solution flowing in a capillary tube, *AIChE Journal*, vol.41(7), 1622-1628.
- Yeo, I. W., M. H. De Freitas, and R. W. Zimmerman (1998), Effect of shear displacement on the aperture and permeability of a rock fracture, *Int. J. Rock Mech. & Min. Sci.*, 35(8), 1051-1070.
-